

Energy & Environmental Science

Accepted Manuscript



This is an *Accepted Manuscript*, which has been through the Royal Society of Chemistry peer review process and has been accepted for publication.

Accepted Manuscripts are published online shortly after acceptance, before technical editing, formatting and proof reading. Using this free service, authors can make their results available to the community, in citable form, before we publish the edited article. We will replace this *Accepted Manuscript* with the edited and formatted *Advance Article* as soon as it is available.

You can find more information about *Accepted Manuscripts* in the [Information for Authors](#).

Please note that technical editing may introduce minor changes to the text and/or graphics, which may alter content. The journal's standard [Terms & Conditions](#) and the [Ethical guidelines](#) still apply. In no event shall the Royal Society of Chemistry be held responsible for any errors or omissions in this *Accepted Manuscript* or any consequences arising from the use of any information it contains.

ARTICLE

The Materials Genome in Action: Identifying the Performance Limits for Methane Storage

Cite this: DOI:
10.1039/x0xx00000x

Received 00th January 2012.
Accepted 00th January 2012

DOI: 10.1039/x0xx00000x

www.rsc.org/

Cory M. Simon,^a Jihan Kim,^b Diego A. Gomez-Gualdron,^c Jeffrey S. Camp,^d Yongchul G. Chung,^c Richard L. Martin,^e Rocio Mercado,^f Michael W. Deem,^g Dan Gunter,^e Maciej Haranczyk,^e David S. Sholl,^d Randall Q. Snurr^{c*} and Berend Smit,^{a,f,h*}

Analogous to the way the Human Genome Project advanced an array of biological sciences by mapping the human genome, the Materials Genome Initiative aims to enhance our understanding of the fundamentals of material science by providing the information we need to accelerate the development of new materials. This approach is particularly applicable to recently developed classes of nanoporous materials, such as metal-organic frameworks (MOFs), which are synthesized from a limited set of molecular building blocks that can be combined to generate a very large number of different structures. In this Perspective, we illustrate how a materials genome approach can be used to search for high-performing adsorbent materials to store natural gas in a vehicular fuel tank. Drawing upon recent reports of large databases of existing and predicted nanoporous materials generated *in silico*, we have collected and compared on a consistent basis the methane uptake in over 650,000 materials based on the results of molecular simulation. The data that we have collected provide candidate structures for synthesis, reveal relationships between structural characteristics and performance, and suggest that it may be difficult to reach the current Advanced Research Project Agency-Energy (ARPA-E) target for natural gas storage.

Broader Context

Natural gas, mostly methane, is an attractive replacement of petroleum fuels for automotive vehicles because of its economic and environmental advantages. However, it suffers from a low volumetric energy density, necessitating densification to yield reasonable driving ranges from a full fuel tank. Densification strategies in the market today, liquefied natural gas (LNG) and compressed natural gas (CNG), require expensive, cumbersome vehicular fuel tanks and refill station infrastructure. If we are able to develop nanoporous material adsorbent to store natural gas at ambient temperature and a moderate pressure, one could envision simple fuel tank that can be refilled at home. Modern, advanced nanoporous materials are highly tunable; inundating researchers with practically infinite possibilities of materials to synthesize and test for methane storage. The current research is focused on finding among these millions of possible materials one that can replace CNG or LNG. In this Perspective, we adopt a computational approach to screen databases of over 650,000 nanoporous material structures. Using this Nanoporous Materials Genome approach, we reveal relationships between structural characteristics and performance, and suggest that it may be difficult, if not impossible, to reach the current Advanced Research Project Agency-Energy (ARPA-E) target for natural gas storage using nanoporous materials.

Introduction

Natural gas, which is mostly methane, is an attractive alternative to petroleum as a transportation fuel because of the increasing supply¹ and possibly lower emissions of greenhouse gases and other pollutants.²⁻⁴ The main technological obstacle for the replacement of gasoline with natural gas is the comparatively low volumetric energy density of natural gas. On a mass basis, the heat of combustion of methane is slightly higher than that of gasoline. However, at ambient conditions, the density of methane is so low that one needs a densification strategy to get an acceptable driving range from a reasonably sized vehicular fuel tank. The current technologies for increasing the density of natural gas – liquefaction or compression – require special infrastructure and incur high energy costs.⁵ Liquefied natural gas (LNG) involves an energy-intensive process of cooling methane to a liquid at ca. 111 K, and the cryogenic fuel tanks required to store LNG onboard are bulky and expensive. Compressed natural gas (CNG) involves compression to 200-300 bar at ambient temperature, requiring costly, multi-stage compressors at refilling stations. To withstand such high pressures, CNG fuel tanks are thick-walled and heavy. Furthermore, the tanks must be cylindrical or spherical to evenly distribute stress. This makes for cumbersome, non-conformable tanks that take up cargo space in the vehicle.⁵

An alternative way to increase the density of natural gas is to pack the fuel tank with a porous material.⁶ The goal is to adsorb methane within the pores to achieve a density competitive with CNG but at a lower storage pressure by exploiting the van der Waals attractions between methane and the pore walls. This lower storage pressure would alleviate the infrastructure barriers of LNG or CNG and allow for lighter, thinner-walled, conformable fuel tanks. The Advanced Research Projects Agency-Energy (ARPA-E) of the US Department of Energy set a target that one volume of adsorbent material should deliver 315 volumes of methane at STP (standard temperature and pressure) to the engine using a storage pressure of 65 bar at ambient temperature. The target was set to be 25% more than the energy density of CNG to anticipate the reduction of the single-crystal deliverable capacity during packing and pelletization.^{7, 8} These targets have generated a significant experimental effort to synthesize and test different nanoporous materials.⁹⁻¹¹ At present, the most promising materials have a deliverable capacity well below the ARPA-E target.^{7, 9, 12} An important practical question is whether any sorbent material can be designed to deliver 315 v STP/v of methane at these conditions, especially given that the ARPA-E target is based solely on economic considerations for competitiveness with CNG.

One of the exciting aspects of advanced nanoporous materials is the analogy with the Human Genome where a small number of building blocks (e.g., amino acids) can be combined to yield the nearly infinite variety of biology. Similarly, by combining different molecular building blocks, researchers have recently obtained unprecedented chemical and geometrical tunability of nanoporous materials, enabling optimization and tailoring for specific applications. For example, for materials such as metal-organic frameworks (MOFs)⁷⁻⁹ or porous polymer networks (PPNs),¹⁰ millions of different materials can, in principle, be synthesized by combining different molecular building blocks in varying topologies (see Fig 1). In practice, however, due to limits on time and resources, only a small set of the possible materials will ever be synthesized and tested as natural gas adsorbents. Similar challenges exist in the development of Li-ion batteries,¹³ solar water-splitters,¹⁴ piezoelectrics,¹⁵ scintillators,¹⁶ photovoltaics,¹⁷ and thermoelectrics.¹⁸ In recognition of this problem, the Materials Genome Initiative is a 100 million dollar effort from the White House that aims to

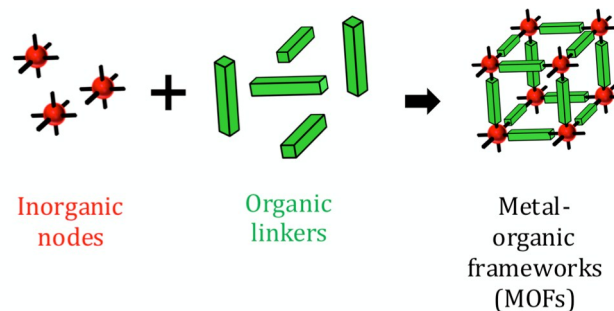


Figure 1: By combining different molecular building blocks, one can obtain an unprecedented large number of materials. For example, inorganic nodes (metals) are combined with organic linkers to form a metal-organic framework (MOF).

“discover, develop, and deploy new materials twice as fast” as current methods.^{19, 20} Part of this initiative is to develop computational tools to explore the vast space of materials and identify those that are optimal for a given application.^{19, 21} In this Perspective, we analyze recent reports from the literature and demonstrate how this approach can address a very practical question: can we find a material that meets the ARPA-E target for methane storage?

Metric for methane storage

There are many important requirements for a material to be a successful candidate for a gas tank adsorbent. At present, it is impossible to take all these factors into account in a screening study. For example, it can be difficult to estimate the costs to synthesize a given material. Screening strategies have therefore focused on the metric that primarily determines the driving range from a given tank volume,⁹ the deliverable capacity. The deliverable capacity is defined as the methane stored per volume of material in a fully loaded tank at the storage pressure, 65 bar, minus the methane that remains at the depletion pressure. The depletion pressure set by ARPA-E, 5.8 bar, was chosen because a sufficient pressure differential must be present to drive flow from the adsorbent to the engine. The deliverable capacity metric takes into account that a material must not only store a large amount of methane at the fuel station; it must also release the methane from the pores when the valve from the tank is open to fuel the engine.

The Nanoporous Materials Genome

Over 3,000,000 different materials have been generated *in silico* by various research groups within the past few years. This set of materials includes libraries of *in silico*-generated zeolites^{22, 23}, MOFs^{24, 25}, zeolitic imidazolate frameworks (ZIFs)²⁶, and PPNs,²⁷ as well as a library of ~5,000 MOFs that have been synthesized.²⁸

Materials

Table 1 summarizes the building blocks and structure of the different classes of porous materials examined in this Perspective. Table 2 illustrates the different strategies used to combine the building blocks to build the structures.

In the Materials Genome approach, we aim to generate models for a large number of structures that are representative for a class of materials. This is, of course, very different from enumerating all possible structures, which would be an impossible aim given the infinite possible combinations of inorganic and organic building blocks. An intuitive strategy for designing new materials is to take inspiration from known experimental materials. In Table 2 we illustrate different

strategies, which apply this concept to generate databases of predicted materials. In the first work of this kind, Wilmer *et al.*²⁴ compiled a set of inorganic secondary building units (SBUs) and bridging organic linkers known from experimental MOF structures and combined these building blocks to generate over 130,000 new MOF structures. In such a scheme, the size of the resulting database can be arbitrarily expanded by the addition of linkers (or metal SBUs), but not all of these might be synthesizable. In a complementary strategy, Martin *et al.*²⁵ used a database of commercially available molecules as a starting point and identified those with the appropriate linker characteristics; this strategy resulted in over 100 analogues of the well-studied MOF-5 system, and more recently, approximately 18,000 new PPN materials.²⁷ A similar strategy was employed to identify alternative imidazole-like substituents for ZIF materials.²⁶ Gomez-Gualdrón *et al.*²⁹ used a small library of building blocks compatible with experimentally observed nets based on the metal SBU of the UiO-66 system,³⁰ –which is renowned for its stability– resulting in over 200 MOF structures. These are examples of “building block selection” strategies for advanced porous materials; we duly note that this terminology does not readily apply to other materials such as zeolites.

The next step in computational materials design is developing an algorithm to combine the organic and/or metallic SBUs to form a particular structure. Here we also see different approaches. Wilmer *et al.*²⁴ defined rules specifying how building blocks may coordinate to one another (much like the limited ways in which Lego bricks may connect) and used a recursive algorithm to exhaustively generate MOF structure models. Martin *et al.*³¹ enumerated highly symmetric crystal topologies consistent with particular SBU combinations and constructed models by positioning the building blocks according to the underlying net. These schemes are not limited to MOFs, and can also be used to generate PPNs, ZIFs and related materials such as covalent organic frameworks (COFs).

An alternative approach was employed for enumeration of novel zeolite structures, which differ in their pore topologies. Deem *et al.*^{22, 23} sampled alternative zeolite topologies by positioning silicon atoms within a unit cell through a Monte Carlo procedure, exploring a wide range of unit cell dimensions and crystal densities for all 230-space groups. Symmetry operations acting on crystallographically unique atoms then generate the full unit cell structure, resulting in 2.6 million topologically distinct zeolite-like structures. The structures were then optimized using a classical force field. Out of the 2.7 million structures, 331,172 were identified to be thermodynamically accessible, i.e., exhibiting energies no more than 30 kJ mol⁻¹-Si above α -quartz. Finally, since ZIFs are a class of MOFs processing the same pore topologies as zeolites, Lin *et al.*²⁶ used the zeolite database to generate a corresponding ZIF database through chemical substitution.

Most experimentally synthesized MOF structures are deposited in the Cambridge Structural Database.³² However, many of these structures contain solvent molecules and other impurities, which makes it very difficult to directly compare these structures with those generated computationally. To make such a comparison possible, Chung *et al.*²⁸ developed computational methods to automatically remove these impurities from the ~5,000 deposited structures; the resulting dataset is known as the computation-ready, experimental (CoRE) MOF database.²⁸ All of these structures are accessible through the Nanoporous Material Website.³³

Properties

To characterize and compare the libraries of different classes of materials, we show in Fig 2 the distributions of their geometric properties. These properties were calculated with the open-source software suite Zeo++,³⁴ which uses a Voronoi decomposition to translate structural information (positions and hard-sphere radii of atoms, size and shape of the periodic unit cell) into a periodic graph representation of the material's porosity. This graph is then analyzed to obtain the accessible surface area and the largest included free sphere. The largest free sphere is defined as the largest hard-sphere that fits in the pore network of the material without overlap with any framework atoms, also modeled as hard-spheres.

Fig. 2 illustrates the large range of geometric properties spanned by these materials. Fig. 2a shows that zeolites typically have the highest crystal densities while PPNs have the lowest; MOFs have a very broad density distribution. Fig. 2b shows that the crystal density correlates inversely with the geometric void fraction, as the most porous materials are generally the least dense. The distribution of pore sizes (Fig. 2c), measured by the largest included hard-sphere that can fit inside the material without overlapping any atoms of the material, mimics the distribution of void fractions as expected from intuition. Fig. 2d shows that PPNs and MOFs tend to achieve the highest surface areas. Characterizing materials by their geometric properties is important because we can link these simple descriptors to the deliverable capacity and elucidate guidelines for material design and selection. Furthermore, these descriptors serve as a multi-dimensional fingerprint that characterizes each material in a high-dimensional space, opening up the possibility for data mining and machine learning techniques to rapidly search this space and predict material performance from simple, easily-computed structural descriptors.^{35, 36}

Screening the Materials Genome

Monte Carlo Simulations

Grand-canonical Monte Carlo simulations have been used in the literature to calculate the adsorption of methane in 650,000 structures in libraries of zeolites,³⁷ MOFs,^{24, 25, 29, 38} and PPNs.²⁷ Some of these studies have used slightly different force fields or pressures. To allow for a direct comparison of these studies, we recomputed the deliverable capacity for these materials. In these calculations, we used the following force fields: UFF³⁹ for PPNs, MOFs, and ZIFs and Dubbeldam *et al.*^{40, 41} for zeolites; TraPPE⁴² for methane. Lorentz-Berthelot mixing rules were used to obtain the solid-adsorbate Lennard-Jones parameters. We used periodic boundary conditions, and the Lennard-Jones potentials were truncated and shifted with a cut-off radius of 12.8Å. We assumed the crystal structures to be rigid, which may induce some errors, as some materials are known to expand and contract with gas adsorption.⁴³⁻⁴⁵ These force fields generally provide good descriptions of most materials in our study (see ESI for a comparison for some structures with experimental data). Notable exceptions are MOFs containing open-metal sites.^{46, 47}

Methane isotherms at 298 K were calculated using a high-performance, parallel algorithm developed for GPUs (graphics processing units), allowing us to compute such a large number of adsorption isotherms in a reasonable time.⁴⁸ The Peng-Robinson equation of state was used to relate the pressure of methane gas to its chemical potential.

Screening

Our initial screening included 650,000 materials: 139,407 predicted zeolite structures^{22, 23} with isotherms from Simon *et al.*³⁷; 137,953 predicted metal-organic framework (hMOF) structures³⁴ of which we made a random selection of 10,000 structures; 17,970 predicted porous polymer network (PPN) structures;²⁷ 381,178 predicted zeolitic imidazolate frameworks (hZIF) structures,²⁶ of which we simulated a random section of 20,000 structures; and a subset of 5,109 Computation-Ready Experimental (CoRE) metal-organic framework structures.²⁸

We computed the deliverable capacity for the initial set of 20,000 hZIFs and 10,000 hMOFs. These calculations showed that the materials with the highest deliverable capacity are described with a largest included sphere in the range 8.0-14.5 Å and have void fractions in the range 0.25-0.7 (See Fig SI-1, in the SI). We then used these criteria on void fractions and largest included spheres to pre-screen the remaining hMOFs and hZIFs for top performers, and added 34,363 hMOF and 37,437 hZIF structures to our final list for which we performed Grand Canonical Monte Carlo simulations.

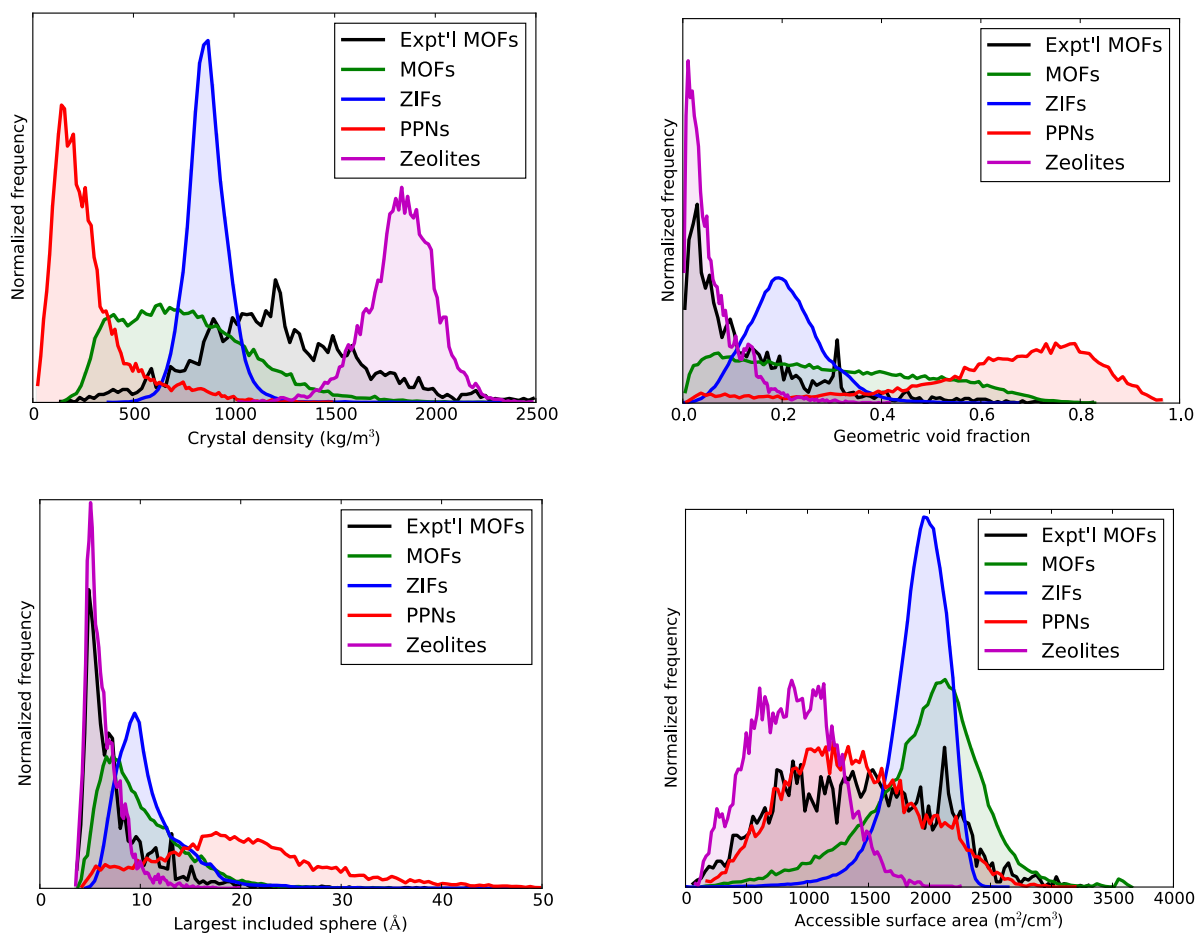


Figure 2: Comparison of the geometric properties in the predicted materials datasets (zeolites, PPNs, ZIFs, and MOFs) and the set of experimental MOFs, as computed from the crystal structures: (top left) crystal density, (top right) geometric void fraction, (bottom left) largest included sphere, (bottom right) accessible surface area. In these histograms we include only those structures that are methane-accessible. A structure is declared methane-accessible (using a methane probe of radius 1.625 Å) if the largest free sphere is greater than the size of our methane probe. We also do not include materials that have deliverable capacities of less than

1

v

STP/v.

Results and discussion

Large datasets such as this can be used to identify promising candidate materials for different applications, assess thermodynamic limits to performance, and elucidate relationships between geometric properties and performance, as illustrated below for natural gas storage.

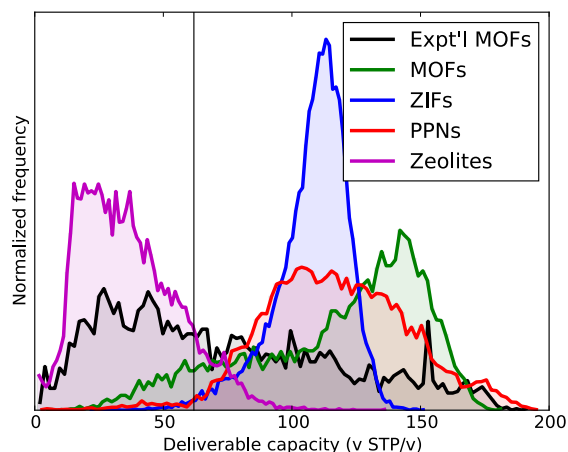


Figure 3: Distribution of the deliverable capacity for different materials; the vertical line marks the deliverable capacity of an empty tank (calculated from the density of bulk methane at 65 bar minus that at 5.8 bar using the Peng-Robinson equation of state)

Fig. 3 shows the distribution of the deliverable capacities of the different materials. Generally, PPNs and MOFs have significantly higher deliverable capacities than zeolites. While the best structures are a significant improvement over the 62 v STP/v deliverable capacity of a free-space tank, no material examined meets the ARPA-E deliverable capacity target. The highest predicted deliverable capacity in the set of 650,000 materials is 196 v STP/v (see ESI, Fig. S5). The materials with the best experimentally measured deliverable capacities to date are MOF-5 (185 v STP/v),⁹ HKUST-1 (185 v STP/v),⁷ UTSA-76 (194 v STP/v),⁴⁹ and MOF-519 (208 v STP/v).¹² Given possible errors in simulation force fields, experimental sample quality, and experimental adsorption measurements, it is striking that extensive experimental and computational work all converge on a maximum deliverable capacity of approximately 200 v STP/v. The very large number of structures examined computationally suggests that the top experimentally tested adsorbents are already at the boundary of the thermodynamic and material performance limits.

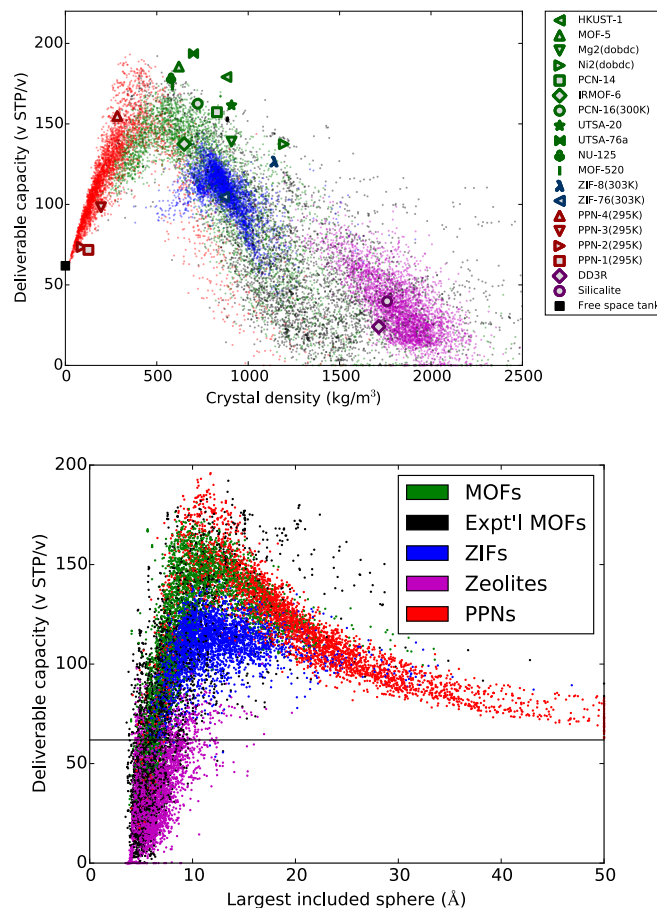


Figure 4: Deliverable capacity for different materials: (top) Relationship between deliverable capacity and crystal density. The symbols are some examples of structures for which we computed the deliverable capacity from the experimental isotherms (see ESI). In all figures, the materials are color-coded according to class. (bottom) Relationship between deliverable capacity and largest included sphere; horizontal line indicates the deliverable capacity of an empty tank. In these scatter plots we include only a random sample of 3,701 structures from each class to avoid cluttering the plots and to assign equal importance to each class of materials.

Analysis of these large datasets in the Materials Genome approach can also provide fundamental insights that are difficult to draw from the limited experimental data. For example, Fig. 4 shows that the materials with the largest deliverable capacities occur in a narrow range of crystal densities. Fig. 4 also shows the relationship between the deliverable capacity and the pore size. We included in Fig. 4 a selection of experimental structures from each material class that exhibit high deliverable capacities and for which experimental methane adsorption isotherms were available. The experimental data generally show the same trends as the simulated data, but the limited number of data points makes it difficult to spot the trends. Fig. 4 illustrates how larger pores increase the capacity to an extent; if the pores become too large, the methane molecules in the middle of the pores do not feel the van der Waals interactions with the walls, and the deliverable capacity approaches that of a free-space tank. The optimal pore diameter of $\sim 11\text{\AA}$ for methane storage is a useful guideline because the size of the molecular building blocks used in synthesis directly controls the pore size.

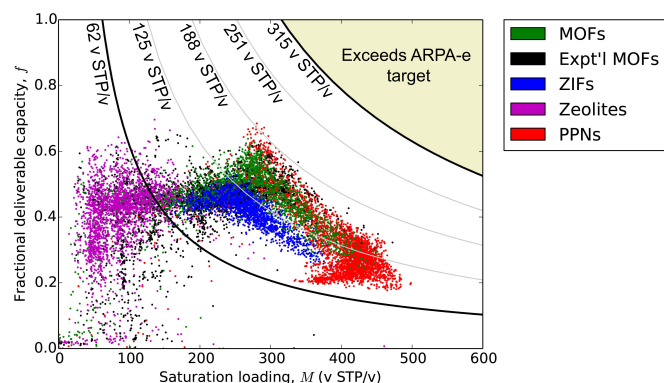


Figure 5: Fractional deliverable capacity f plotted against the saturation loading M for each material. Hyperbolas indicate lines of constant deliverable capacity. The bottom and top hyperbolas give the deliverable capacity of a free space tank and the ARPA-E target, respectively; the region exceeding the ARPA-E target is highlighted in yellow.

Fundamental physical models are an important complement to the “big-data” approach of plots as presented in Fig. 4. An empirical formula for methane storage of MOF materials has been developed by Kong *et al.*⁵⁰ and He *et al.*⁵¹ For example, Simon *et al.*³⁷ developed a statistical thermodynamic model in which the deliverable capacity of a material is viewed as the product of the number of effective adsorption sites per volume, M , and the fractional deliverable capacity f . The fractional deliverable capacity is maximal if the energetics of the adsorption sites is optimal; if the adsorption of methane is too strong, too much methane remains in the tank at the discharge pressure, and, if the adsorption is too weak, too little methane will be in the tank at the storage pressure.^{37, 52} In Fig. 5, we plot the fractional deliverable capacity f of each material against the saturation loading, M (see ESI for details). A hyperbola $f = \sigma_{del}/M$ is a curve of constant deliverable capacity σ_{del} . If the adsorbent in the fuel tank were filled at infinite pressure and depleted by pulling a vacuum to remove all residual methane, all sites would be fully utilized and the deliverable capacity would be equal to the saturation loading (M). However, the adsorption sites may not be fully occupied at 65 bar, and some methane will remain in the pores at 5.8 bar; therefore even for an optimal material, the deliverable capacity is only some fraction f of the saturation loading. For all material classes, we find similar behavior in Fig. 5. For low M (~ 350 v STP/v), there are many materials that have adsorption sites with the optimal methane affinity, endowing the material with a maximal fractional deliverable capacity. However, there is a tradeoff between the density of adsorption sites and the density of the material, such that in the case of high M , we reach an effective density of sites where none of the materials have sites that have optimal affinities for methane. We can only increase the number of adsorption sites if we decrease the number of framework atoms. Lowering the density of framework atoms causes the additional adsorption sites to have little or no interactions with the framework. Hence, the deliverable capacity of these materials approaches that of an empty tank.

From these data, we can identify the ideal material for methane storage: the material with the largest density of adsorption sites under the constraint that the sites have optimal methane interactions. The distinguishing characteristic between different classes of materials is the number of atoms that are involved in creating an optimal adsorption site. Fig. 4 shows that PPNs and MOFs perform better than zeolites and ZIFs, as the former require fewer atoms to create optimal adsorption sites.

An intriguing question is whether a material exists that meets the ARPA-E target. The experimental results to date and computational screening of over 650,000 structures suggest that there may be a physical limitation on the deliverable capacity,

around 200 v STP/v, which is quite far from the ARPA-E target of 315 v STP/v. Adopting a Materials Genome approach allowed this conclusion to be reached rather quickly. Note that the computational studies that provided the data in Figs 2-5 were all published in the past 2 years. Given this tentative conclusion, we can ask whether some other set of operating temperatures and pressures might, then, make adsorbed natural gas tanks more attractive. With the computational infrastructure in place, we can readily recalculate the deliverable capacity for other conditions. For example, in Figs. S8 and S9 (see ESI) we show how changing the loading and delivery pressures affect the deliverable capacity. Another interesting option is to re-engineer the tank to use residual heat from the engine to drive off the residual methane at the delivery pressure.³⁸ Fig. 6 shows that by discharging at a higher temperature, one can significantly increase the deliverable capacity. We also see that the shape of the distribution changes. The reason being that a different set of materials is optimal for different storage conditions (Figs. S8-S9, see ESI). For example, a lower discharge pressure or higher discharge temperature favors materials that have stronger interactions with methane, while a higher storage pressure favors materials with a larger pore volume and weaker interactions. Still, none of these more favorable storage conditions allow materials to reach the ARPA-e target.

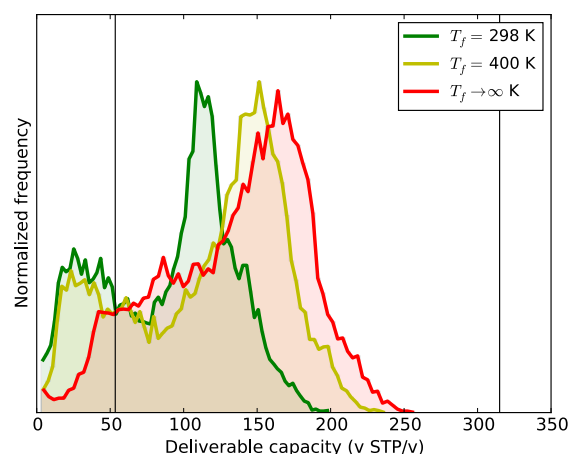


Figure 6: Amending the storage conditions and tank design changes the deliverable capacity. The distribution of deliverable capacities between 65 and 5.8 bar for ambient temperature operation (green), when the adsorbent is heated to $T_f = 400$ K when nearing discharge (yellow), and when all residual gas is driven off (red). In the last scenario, the deliverable capacity is equal to the high-pressure loading. Vertical lines denote the deliverable capacity of an empty tank and the ARPA-E target.

Conclusions

Screening hundreds of thousands of different materials gives us new insights that cannot be obtained otherwise. First of all, the Materials Genome approach allows us to explore a much larger range of materials than researchers could ever synthesize and is therefore ideal to obtain insights into the limits of an entire class of materials and into structure/performance relationships. In the past, if we wanted to know how methane uptake correlates with, for example, crystal density, we might measure or simulate the properties of a dozen materials and look for a simple linear correlation. Now, with hundreds of thousands of structures, we obtain a much more complete insight into the full complexity of this question, as shown in Fig. 4. In addition, the huge amount of data generated in high-throughput screening opens opportunities for data mining as a tool to extract additional, possibly unexpected relationships between material characteristics and performance. For example, in Fig. 5, we can visualize the relation between pore size and deliverable capacity with a simple scatter plot. As we see drastically

different deliverable capacities for a given pore size, it is clear that certain combinations of properties are required and thus including other descriptors will add predictive value. In such a high-dimensional space, machine-learning techniques are useful for extracting complicated relationships and making more accurate performance predictions from structural descriptors.

Although hundreds of thousands of predicted nanoporous materials have been generated within the past few years, the chemical search space is so large that all possible structures cannot be enumerated. Fig. 2 shows that the experimental MOF structures have different crystal density and surface area distributions than structures in the predicted MOF database. These differences raise questions about how to ensure that the chemical space is adequately sampled. In addition, only a subspace of all possible materials can ever be synthesized. An interesting application of material genomics would be to identify the feasibility of synthesizing a given material.

From the screening studies summarized here, we conclude that the classes of materials currently being investigated are unlikely to meet the ARPA-E target for natural gas storage. This is not surprising as the ARPA-E target was not based on thermodynamic or material arguments but rather based on economic competition with CNG. High-throughput screening allowed an assessment about the feasibility of the target in a very short period of time, allowed alternative operating scenarios to be quickly evaluated, and provided useful structure/performance relationships. This is an illustrative example of how a Materials Genome approach can drastically reduce experimental time and effort by eliminating unproductive tasks and focusing experimental efforts on the most interesting candidates.

An important practical question is whether an energy density of ca. 200 v STP/v under the currently proposed storage conditions is sufficient to justify the adoption of vehicular adsorbed natural gas fuel tanks. However, natural gas storage is not the only application of nanoporous materials. These materials are also of interest for other gas separations,⁵³ including CO₂ capture,⁵⁴ gas sweetening,⁵⁵ separations of hydrocarbons,⁵⁶ membranes,⁵⁷ catalysis,⁵⁸ sensors,⁵⁹ and drug delivery⁶⁰. For these applications, one can screen the databases discussed in this Perspective to reveal any performance limits, identify specific materials with exceptional properties, and elucidate relationships between material characteristics and performance use data mining techniques.

Acknowledgements

The research was supported by the U.S. Department of Energy, Office of Basic Energy Sciences, Division of Chemical Sciences, Geosciences and Biosciences under Award DE-FG02-12ER16362.

Notes and references

^a Department of Chemical and Biomolecular Engineering, University of California, Berkeley, Berkeley, CA 94720-1462, USA

^b Department of Chemical and Biomolecular Engineering, Korea Advanced Institute of Science and Technology, 291 Daehak-ro Yuseong-gu Daejeon, Korea 305-701

^c Department of Chemical and Biological Engineering, Northwestern University, Evanston, IL 60208 USA

^d School of Chemical & Biomolecular Engineering, Georgia Institute of Technology, Atlanta, GA, 30332 USA

^e Computational Research Division, Lawrence Berkeley National Laboratory, Berkeley, CA 94720-8139, USA

^f Department of Chemistry, University of California, Berkeley, Berkeley, CA 94720-1462, USA

^g Departments of Bioengineering and Physics & Astronomy, Rice University, Houston, TX 77005, USA

^h Laboratory of molecular simulation, Institut des Sciences et Ingénierie Chimiques, Ecole Polytechnique Fédérale de Lausanne (EPFL), CH-1015 Lausanne, Switzerland

Electronic Supplementary Information (ESI) available: includes the additional data mentioned in the text See DOI: 10.1039/b000000x/

1. S. Chu and A. Majumdar, *Nature*, 2012, **488**, 294-303.
2. M. Q. Wang and H. S. Huang, *A full fuel-cycle analysis of energy and emissions impacts of transportation fuels produced from natural gas*, Report ANL/ESD-40; TRN: AH200002%38 United States 10.2172/750803TRN: AH200002%38 Tue Feb 05 03:46:35 EST 2008ANL; EDB-00:004527English, 2000.
3. R. W. Howarth, R. Santoro and A. Ingraffea, *Climatic Change*, 2011, **106**, 679-690.
4. R. A. Alvarez, S. W. Pacala, J. J. Winebrake, W. L. Chameides and S. P. Hamburg, *P Natl Acad Sci USA*, 2012, **109**, 6435-6440.
5. S. Yeh, *Energy Policy*, 2007, **35**, 5865-5875.
6. V. C. Menon and S. Komarneni, *J Porous Mat*, 1998, **5**, 43-58.
7. Y. Peng, V. Krungleviciute, I. Eryazici, J. T. Hupp, O. K. Farha and T. Yildirim, *J Am Chem Soc*, 2013, **135**, 11887-11894.
8. K. Konstas, T. Osl, Y. X. Yang, M. Batten, N. Burke, A. J. Hill and M. R. Hill, *J Mater. Chem.*, 2012, **22**, 16698-16708.
9. J. A. Mason, M. Veenstra and J. R. Long, *Chem. Soc. Rev.*, 2014, **5**, 32-51.
10. T. A. Makal, J.-R. Li, W. Lu and H.-C. Zhou, *Chem. Soc. Rev.*, 2012, **41**, 7761-7779.
11. Y. B. He, W. Zhou, G. D. Qian and B. L. Chen, *Chem Soc Rev*, 2014, **43**, 5657-5678.
12. F. Gandara, H. Furukawa, S. Lee and O. M. Yaghi, *J Am Chem Soc*, 2014, **136**, 5271-5274.
13. H. L. Chen, G. Hautier, A. Jain, C. Moore, B. Kang, R. Doe, L. J. Wu, Y. M. Zhu, Y. Z. Tang and G. Ceder, *Chem Mater*, 2012, **24**, 2009-2016.
14. I. E. Castelli, D. D. Landis, K. S. Thygesen, S. Dahl, I. Chorkendorff, T. F. Jaramillo and K. W. Jacobsen, *Energ Environ Sci*, 2012, **5**, 9034-9043.
15. R. Armiento, B. Kozinsky, M. Fornari and G. Ceder, *Phys Rev B*, 2011, **84**.
16. C. Ortiz, O. Eriksson and M. Klintonberg, *Comp Mater Sci*, 2009, **44**, 1042-1049.
17. L. P. Yu and A. Zunger, *Phys Rev Lett*, 2012, **108**.
18. S. D. Wang, W. Setyawan, N. Mingo and S. Curtarolo, *Phys Rev X*, 2011, **1**.
19. A. Jain, S. P. Ong, G. Hautier, W. Chen, W. D. Richards, S. Dacek, S. Cholia, D. Gunter, D. Skinner, G. Ceder and K. A. Persson, *APL Mat.*, 2013, **1**, -.
20. T. Kali and C. Wadia, <http://www.whitehouse.gov/blog/2011/06/24/materials-genome-initiative-renaissance-american-manufacturing>.
21. T. Kalil and C. Wadia, The National Science and Technology Council, Washington, 2011.
22. M. W. Deem, R. Pophale, P. A. Cheeseman and D. J. Earl, *J. Phys. Chem. C*, 2009, **113**, 21353-21360.
23. R. Pophale, P. A. Cheeseman and M. W. Deem, *Phys Chem Chem Phys*, 2011, **13**, 12407-12412.
24. C. E. Wilmer, M. Leaf, C. Y. Lee, O. K. Farha, B. G. Hauser, J. T. Hupp and R. Q. Snurr, *Nat Chem*, 2012, **4**, 83-89.
25. R. L. Martin, L.-C. Lin, K. Jariwala, B. Smit and M. Haranczyk, *J Phys Chem C*, 2013, **117**, 12159-12167.
26. L.-C. Lin, A. H. Berger, R. L. Martin, J. Kim, J. A. Swisher, K. Jariwala, C. H. Rycroft, A. S. Bhowm, M. W. Deem, M. Haranczyk and B. Smit, *Nat. Mater.*, 2012, **11**, 633-641.
27. R. L. Martin, C. M. Simon, B. Smit and M. Haranczyk, *J. Am. Chem. Soc.*, 2014, **136**, 5006-5022.
28. Y. G. Chung, J. Camp, M. Haranczyk, B. Sikora, D. S. Sholl and R. Q. Snurr, *Chem. Mater.*, 2014, DOI: 10.1021/cm502594j.
29. D. A. Gomez-Gualdrón, O. V. Gutov, V. Krungleviciute, B. Borah, J. E. Mondloch, J. T. Hupp, T. Yildirim, O. K. Farha and R. Q. Snurr, *Chem. Mater.*, 2014, **26**, 5632-5639.

30. J. H. Cavka, S. Jakobsen, U. Olsbye, N. Guillou, C. Lamberti, S. Bordiga and K. P. Lillerud, *J. Am. Chem. Soc.*, 2008, **130**, 13850-13851.
31. R. L. Martin and M. Haranczyk, *Crys. Growth Des.*, 2014, **14**, 2431-2440.
32. F. H. Allen, *Acta Crystallogr B*, 2002, **58**, 380-388.
33. M. Haranczyk, Nanoporous Materials Database, <http://nanoporousmaterials.org/methanestorage/>.
34. T. F. Willems, C. Rycroft, M. Kazi, J. C. Meza and M. Haranczyk, *Microporous Mesoporous Mat.*, 2012, **149**, 134-141.
35. T. Le, V. C. Epa, F. R. Burden and D. A. Winkler, *Chem Rev*, 2012, **112**, 2889-2919.
36. M. Fernandez, T. K. Woo, C. E. Wilmer and R. Q. Snurr, *J. Phys. Chem. C.*, 2013, **117**, 7681-7689.
37. C. M. Simon, J. Kim, L. C. Lin, R. L. Martin, M. Haranczyk and B. Smit, *Phys. Chem. Chem. Phys.*, 2014, **16**, 5499-5513.
38. D. A. Gómez-Gualdrón, C. E. Wilmer, O. K. Farha, J. T. Hupp and R. Q. Snurr, *J. Phys. Chem. C.*, 2014, **118**, 6941-6951.
39. A. K. Rappe, C. J. Casewit, K. S. Colwell, W. A. Goddard and W. M. Skiff, *J. Am. Chem. Soc.*, 1992, **114**, 10024-10035.
40. D. Dubbeldam, S. Calero, T. J. H. Vlugt, R. Krishna, T. L. M. Maesen, E. Beerdsen and B. Smit, *Phys. Rev. Lett.*, 2004, **93**, art no. 088302.
41. D. Dubbeldam, S. Calero, T. J. H. Vlugt, R. Krishna, T. L. M. Maesen and B. Smit, *J. Phys. Chem. B*, 2004, **108**, 12301 - 12313.
42. M. G. Martin and J. I. Siepmann, *J. Phys. Chem. B*, 1998, **102**, 2569--2577.
43. C. Serre, F. Millange, C. Thouvenot, M. Nogues, G. Marsolier, D. Louer and G. Férey, *J Am Chem Soc*, 2002, **124**, 13519-13526.
44. L. Sarkisov, R. L. Martin, M. Haranczyk and B. Smit, *J. Am. Chem. Soc.*, 2014, **136**, 2228-2231.
45. F. X. Coudert, A. Boutin and A. H. Fuchs, *Mol Phys*, 2014, **112**, 1257-1261.
46. R. B. Getman, Y.-S. Bae, C. E. Wilmer and R. Q. Snurr, *Chem. Rev.*, 2012, **112**, 703-723.
47. A. Dzubak, L.-C. Lin, J. Kim, J. A. Swisher, R. Poloni, S. N. Maximoff, B. Smit and L. Gagliardi, *Nat Chem*, 2012, **4**, 810-816.
48. J. Kim and B. Smit, *J. Chem. Theory Comput.*, 2012, **8**, 2336-2343.
49. B. Li, H. M. Wen, H. L. Wang, H. Wu, M. Tyagi, T. Yildirim, W. Zhou and B. L. Chen, *J Am Chem Soc*, 2014, **136**, 6207-6210.
50. G. Q. Kong, Z. D. Han, Y. B. He, S. Ou, W. Zhou, T. Yildirim, R. Krishna, C. Zou, B. L. Chen and C. D. Wu, *Chem-Eur J*, 2013, **19**, 14886-14894.
51. Y. B. He, W. Zhou, T. Yildirim and B. L. Chen, *Energ Environ Sci*, 2013, **6**, 2735-2744.
52. S. K. Bhatia and A. L. Myers, *Langmuir*, 2006, **22**, 1688-1700.
53. J.-R. Li, J. Sculley and H.-C. Zhou, *Chem. Rev.*, 2012, **112**, 869-932.
54. K. Sumida, D. L. Rogow, J. A. Mason, T. M. McDonald, E. D. Bloch, Z. R. Herm, T.-H. Bae and J. R. Long, *Chem. Rev.*, 2012, **112**, 724-781.
55. J. Kim, A. Maiti, L.-C. Lin, J. K. Stolaroff, B. Smit and R. D. Aines, *Nat Commun*, 2013, **4**, 1694.
56. E. D. Bloch, W. L. Queen, R. Krishna, J. M. Zadrozny, C. M. Brown and J. R. Long, *Science*, 2012, **335**, 1606-1610.
57. Y. Dai, J. R. Johnson, O. Karvan, D. S. Sholl and W. J. Koros, *J. Memb. Sci.*, 2012, **401-402**, 76-82.
58. J. Lee, O. K. Farha, J. Roberts, K. A. Scheidt, S. T. Nguyen and J. T. Hupp, *Chem. Soc. Rev.*, 2009, **38**.
59. L. E. Kreno, K. Leong, O. K. Farha, M. Allendorf, R. P. Van Duyne and J. T. Hupp, *Chem. Rev.*, 2012, **112**, 1105-1125.
60. S. T. Meek, J. A. Greathouse and M. D. Allendorf, *Adv. Mater.*, 2011, **23**, 249-267.

Table 1. Materials studied in this work. MOFs, PPNs, zeolites and ZIFs are described in terms of their constituent building blocks and resulting topologies. The “Building blocks” column illustrates both symbolic representations of the geometry of possible building blocks (above) and chemical examples thereof (below). Similarly, the “Topologies” column provides graph representations (nets) of possible topologies for each material class (above) and examples of chemical structures exhibiting these topologies (below). Solid vertical lines distinguish between classes of building block (e.g., metal-organic versus organic) or types of topology; note also that in some cases, many more possibilities exist beyond the few illustrated.

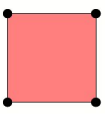
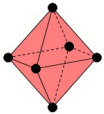

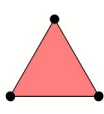
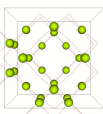
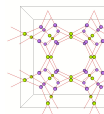
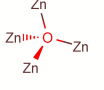
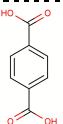
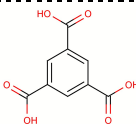
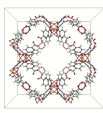
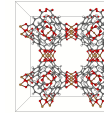
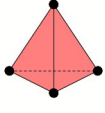

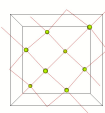
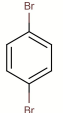
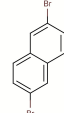
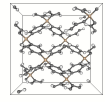
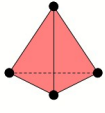

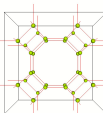
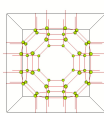
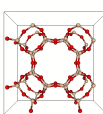
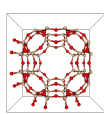
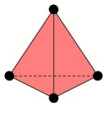

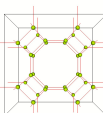
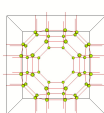
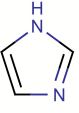
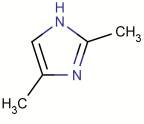
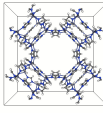
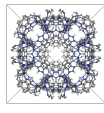
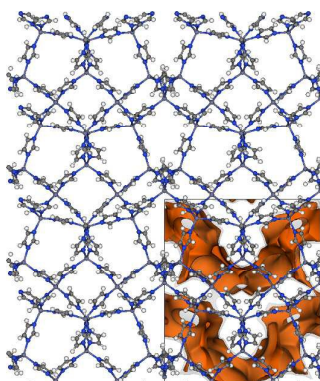
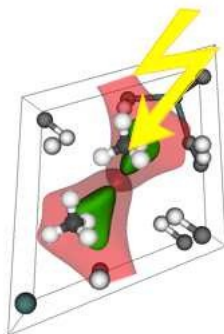
Material class	Building blocks				Topologies	
MOFs						
	Cu—Cu					
PPNs						
	Si	Ge				
Zeolites						
	Si		O			
ZIFs						
	Zn	Fe				

Table 2. The complementary strategies employed to navigate the vast chemical space of possible nanoporous materials, exemplified by the specific datasets discussed in this work. Each strategy comprises a “Building block selection” and “Model construction” component, as described.

Name of material dataset	Building block selection strategy		Model construction strategy
MOFs			<p>Modes of coordination between building blocks are specified; recursive algorithm combines building blocks in permissible combinations and infers a unit cell</p>
MOF-5s			<p>Based on the underlying net of MOF-5 (pcu), building blocks are positioned in space and symmetry operations complete the unit cell; structures subsequently relaxed with semi-empirical PM6-DH2</p>
PPNs			<p>Based on the underlying net of PPN (dia), building blocks are positioned in space and symmetry operations complete the unit cell; structures subsequently relaxed with semi-empirical PM6-DH2</p>
Zeolites	<p>Tetrahedrally-coordinated silicon atoms, bridged by oxygen atoms</p>		<p>For each symmetry space group and a variety of unit cell parameters, Si atoms are positioned via a Monte Carlo process; symmetry operations complete the unit cell and bridging oxygens are placed; structures are subsequently relaxed with one of two interatomic potentials</p>
ZIFs			<p>Tetrahedrally-coordinated zinc atoms, bridged by imidazolate linkers</p> <p>M - IM - M Si - O - Si 1 2</p>
ZIFs (decorated)			<p>For each zeolite topology, the Si-O-Si motif is replaced by a Zn-Im-Zn motif (Im being an imidazolate-like group), the unit cell is scaled by 1.95x compared to the original zeolite</p>

Graphical abstract

Best ZIF structure found in screening of databases containing over half a million nanoporous materials for vehicular methane storage.



SUPPLEMENTARY INFORMATION

The Materials Genome in Action: Identifying the Performance Limits for Methane Storage

Cory M. Simon, Jihan Kim, Diego A. Gomez-Gualdron, Jeffrey S. Camp,
Yongchul G. Chung, Richard L. Martin, Rocio Mercado, Michael Deem,
Dan Gunter, Maciej Haranczyk, David S. Sholl, Randall Q. Snurr, Berend
Smit

December 19, 2014

S1 Screening the database

Fig. S1 gives a scatter plot of the deliverable capacity of the training set against the largest included sphere. The structures with the highest deliverable capacities have largest included spheres that fall in $[8.0, 14.5\text{\AA}]$, shown as the interval bracketed by the blue, vertical lines. The color-coding of the points in Fig. S1 indicates the void fraction. As all green points have void fractions outside of $[0.25, 0.7]$, we see that the structures with the highest deliverable capacities also have void fractions in the interval $[0.25, 0.7]$.

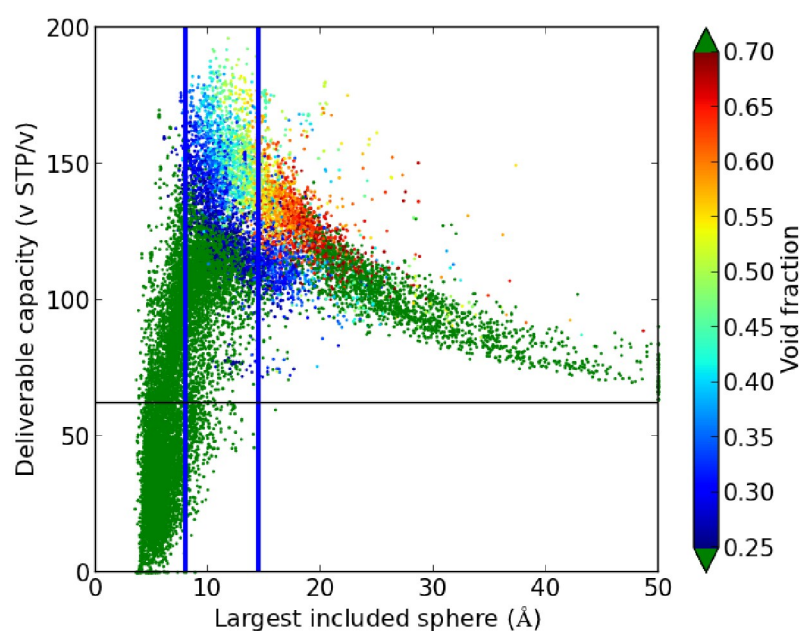


Figure S1. Screening strategy with geometric descriptors. Deliverable capacity plotted against the diameter of the largest included sphere. Color indicates geometric void fraction. We computed methane adsorption isotherms of all structures falling between the two vertical blue lines and having a void fractions between 0.25 and 0.70.

S2 Comparison with experimental data

To test the reliability of our methodology, we compared the methane adsorption isotherms of experimental structures that were available in the literature to the analogous structures in our dataset. Using Grand-canonical Monte Carlo simulations, we simulated the isotherms for HKUST-1 (see Fig. S2); Mg-MOF-74, Ni-MOF-74, and Co-MOF-74 (see Fig. S3); and MOF-5 and PCN-14 (see Fig. S4) from 0 to 80 bar at 298 K.

For PCN-14 and MOF-5, our simulations give a good agreement with the experimental data. For the MOF-74 series, it is known that not all open metal sites are activated [1], giving a lower maximum adsorption compared to the perfect crystal structures used in our simulations. To correct for these blocked adsorption sites, we scaled the isotherms by the ratio of normalized surface areas in Mg-, Co-, and Ni-MOF-74, as reported in Table 2 of Ref. [2], where the surface areas are derived from a Langmuir fit of 77K N₂ adsorption isotherms. In the case of Zn-MOF-74, $\approx 24\%$ of the surface area, and thus binding sites, is not accessible; in Ni-MOF-74, $\approx 10\%$; in Mg-MOF-74, $\approx 13\%$; and in Co-MOF-74, $\approx 18\%$ of binding sites are not accessible. We see that in frameworks with these particularly strong binding sites, such as Ni-MOF-74 and HKUST-1, the UFF + TraPPE force field underestimates the adsorption isotherms.

In conclusion, our force field tends to slightly underestimate the measured methane uptake in certain materials, by anywhere from 7% (MOF-5) to 20% (Ni-MOF-74) at 65 bar, which explains why in our screening study our top performing structures have a slightly lower deliverable capacity compared to the experimental structures.

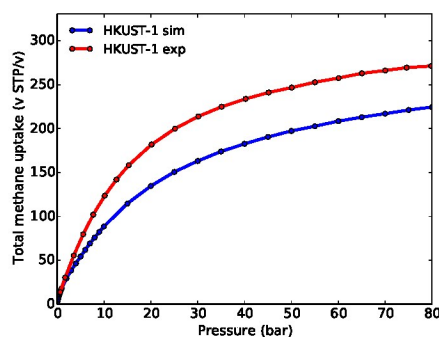


Figure S2. Adsorption isotherm of methane in HKUST-1. The experimental data are from Mason *et al.* [1].

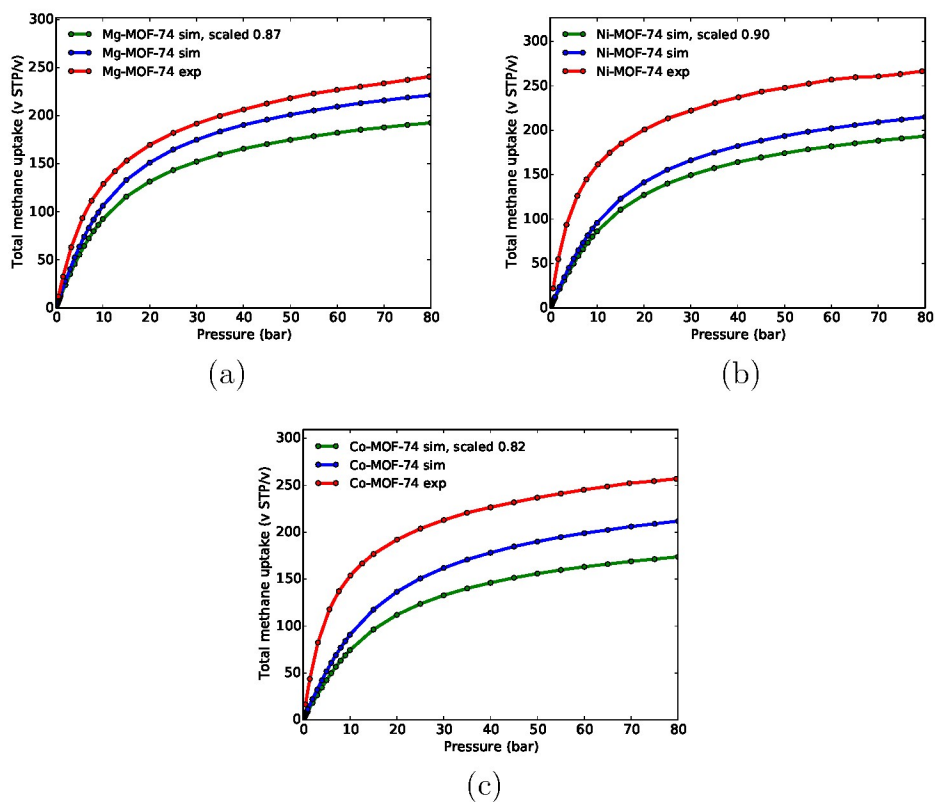


Figure S3. Adsorption isotherm of methane in (a) Mg-MOF-74, (b) Ni-MOF-74, and (c) Co-MOF-74. The experimental data are from Mason *et al.* [1]. The simulated isotherms are scaled to take into account that in the experimental structures not all open metal sites are accessible.

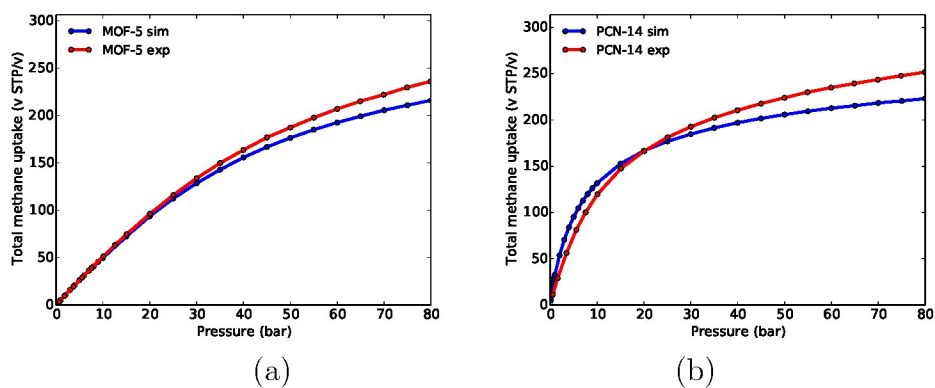


Figure S4. Adsorption isotherm of methane in (a) MOF-5 and (b) PCN-14. The experimental data are from Mason *et al.* [1].

S3 Top material for methane storage

The material with the highest predicted deliverable capacity in our study is a hypothetical porous polymer network (PPN), Adamantane 4387 1-net 004 [3], exhibiting a 65 - 5.8 bar deliverable capacity of 196 v STP/v. The structure is shown in Fig. S5. We plotted the potential energy contours of a methane molecule in the pores at -12 kJ/mol (orange) and 0 kJ/mol (gray) to highlight the binding regions. This material exhibits a largest included sphere of 11.75 Å; this is larger than a single methane molecule. The strong binding regions in orange indicate that multiple methane molecules can be efficiently packed into the pores. The computed surface area of this material is 1992 m²/cm³.

This PPN can in principle be synthesized from known synthesis routes [4] using an adamantane core and 1,2-dibromoethylene linkers: Four of these linkers are appended to each tetrahedral point of the adamantane cage. When two of these tetrahedral monomers then react, we get the C₄H₄ linkage spanning the adamantane cages. This ‘two-monomer synthesis route’ is discussed in detail in Ref. [3].

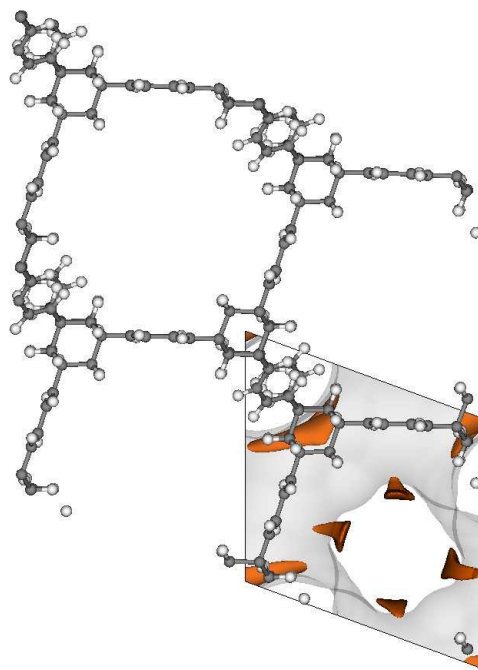


Figure S5. Adamantane 4387 1-net 004 exhibits a 65 - 5.8 bar methane deliverable capacity of 196 v STP/v. Contours of the potential energy of a methane molecule in the pores are shown at -12 kJ/mol (orange) and 0 kJ/mol (gray).

S4 Estimating the saturation loading M

To estimate the saturation methane loading in each material, which we call the effective density of adsorption sites, we fit the simulated methane adsorption isotherms from 1 – 160 bar fugacity to model 1 in Ref. [5], which builds upon a Langmuir model by including adsorbate-adsorbate interactions. The model is a Langmuir model at first order, with a correction term that is weighted by the strength of the adsorbate-adsorbate interactions (θ) [5]

$$\frac{\sigma}{M} = \frac{\frac{K_H}{M} \phi P}{1 + \frac{K_H}{M} \phi P} + \theta \left(\frac{\frac{K_H}{M} \phi P}{1 + \frac{K_H}{M} \phi P} \right)^2 \left(\frac{\frac{K_H}{M} \phi P}{1 + \frac{K_H}{M} \phi P} - 1 \right). \quad (\text{S1})$$

The variable σ is the methane loading per volume of material; M is the saturation loading or effective density of sites; K_H is the Henry coefficient; P is the pressure; ϕ is the fugacity coefficient such that ϕP is the fugacity of methane corresponding to pressure P . The Henry coefficient in eqn S1 is independently obtained from the Widom insertion method. We thus fit each methane adsorption isotherm to the model in eqn S1 using the parameters M and θ with a nonlinear least squares data fitting routine implemented with the `OPTIMIZE` function in Scipy, an open-source computing package in Python. If the highest-pressure point in the simulated isotherm (160 bar fugacity) was less than 60% of the identified M , we extended the isotherms to a fugacity of 700 bar to obtain enough curvature in the simulated isotherms for our fitting routine to reliably estimate M . For plots involving M , we only include structures whose residual sum of squares (including all 14 data points on the isotherm) is below 5% of M to help ensure the estimation of M is reliable.

S5 Literature survey for experimental methane adsorption isotherms

We searched the literature for high-performing structures in each material class for which experimentally measured methane adsorption isotherms were available. Where noted, we took the total adsorption; otherwise, we converted the excess adsorption into total using the reported pore volume and the density of methane from the Peng-Robinson equation of state. These data are depicted in Fig. 4 of the main text.

The model in eqn S1 was fitted to the experimental adsorption isotherms to interpolate methane adsorption for the relevant pressures when the experimental measurement was not taken at exactly 5.8 and 65 bar. The experimental data were taken from the following references: MOF-519 and MOF-520 [6]; HKUST-1, Mg2(dobdc), Ni2(dobdc), MOF-5, PCN-14 [1]; IRMOF-6 [7]; PCN-16, [8]; NU-125, UTSA-20 [9]; ZIF-8, ZIF-76, [10]; PPN-4 [11]; PPN-1, PPN-2, PPN-3 [12]; DD3R [13]; and Silicate for crystal density [14].

S6 Alternative Operating Conditions

Here, we outline our methods for calculating the deliverable capacity of our materials under different conditions than set in the ARPA-E target. To avoid having to carry out simulations at many different temperatures and pressures, we characterize each material by the parameters M , K_H , and θ obtained from fitting the simulated isotherms at 298 K to the model in eqn S1. To extrapolate the loading at a higher temperature, we assume that the temperature dependence of the Henry coefficient K_H is given by the Van't Hoff equation and the temperature dependence of θ (see Ref. [5]):

$$K_H \sim e^{-\frac{\Delta H}{RT}} \quad (\text{S2})$$

$$\theta \sim \frac{1}{T}. \quad (\text{S3})$$

We calculated the enthalpy of adsorption ΔH (= negative of the heat of adsorption) during our simulations. We subsequently use these parameters to estimate the methane adsorption at alternative conditions.

To test that the various predictions made with these fitted parameters gives a sufficiently accurate description of the isotherms that would be obtained by simulations we carried out several tests. In Fig. S6 we show that the fitted isotherms describe the simulated deliverable capacity sufficiently accurate. Fig. S7 shows that this approach gives a sufficiently accurate description of the methane adsorption isotherms at these different temperatures.

S6.1 Altering the operation conditions

In the calculations that follow, we include a random sample of 3,701 materials from each class to assign each class an equal prior. We amalgamate all material classes together and plot the distribution of deliverable capacities at the different storage conditions. For each alternative operating condition, we also depict how one class of materials may perform better over another class at different conditions by stacking the probability distributions for each class. This allows us to visualize the contributions of each material class to the probability distributions.

We now assess the impact of changing the operating pressures on the deliverable capacity at 298 K. Methane is stored in the adsorbed natural gas tank at P_H bar at the refilling station, and a tank is considered depleted if it exhibits a pressure of P_L bar. By changing P_H and P_L , we compute the deliverable capacity under two scenarios that will benefit the deliverable capacity: (i) Increasing the storage pressure P_H but keeping the ARPA-E target's discharge pressure of $P_L = 5.8$ bar (ii) Decreasing the discharge pressure P_L but keeping the ARPA-E target's storage pressure of $P_H = 65$ bar.

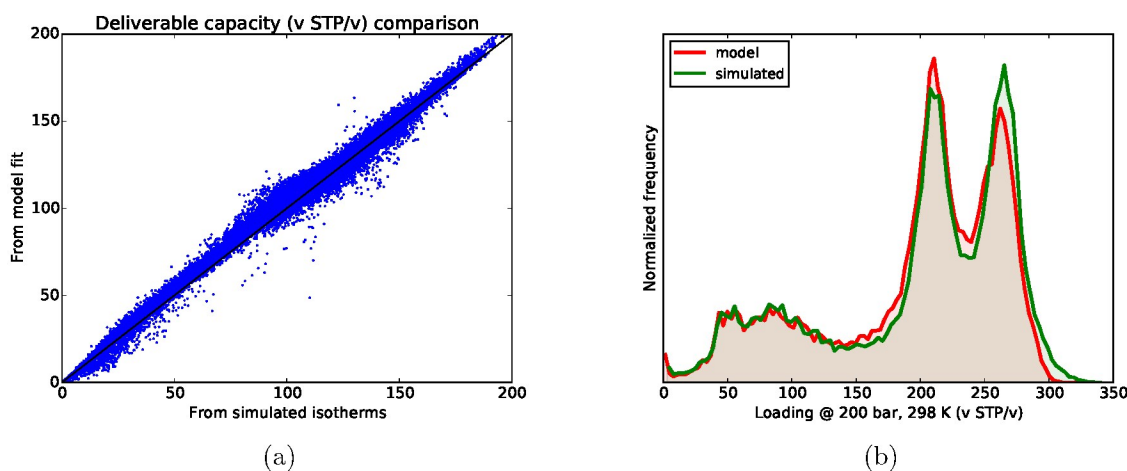


Figure S6. Validating the approximation of isotherms with the model in eqn. S1. (a) For each material, we plotted the deliverable capacities at 298 K between 65 and 5.8 bar obtained from the model fit against that obtained from the simulated isotherm. The points follow the diagonal with a modest variance. (b) We compare the distribution of 200 bar loadings using the simulated loading and the fitted model.

S6.1.1 Altering the storage pressure

Fig. S8 shows how the distribution of deliverable capacities is changing if we increase the storage pressure $P_H = 65, 100, 150,$ and 200 bar. As expected, the higher the storage capacity the larger the deliverable capacity; however, even at 200 bar we do not reach the ARPA-E target.

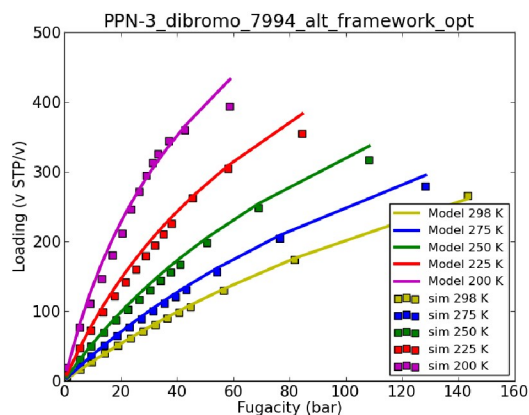
S6.1.2 Altering the discharging pressure

Fig. S9 shows the effects of decreasing the recharging pressure $P_L = 5.8, 3, 1,$ and 0 bar, while keeping the charging pressure $P_H = 65$ bar. In these calculations the deliverable capacity with $P_L = 0$ is equal to the loading at $P_H = 65$ bar. As expected, decreasing the discharging pressure increases the deliverable capacity. In particular materials for which methane is strongly bound will have a higher deliverable capacity.

S6.1.3 Heat rerouting deliverable capacity

In the main text, we investigate the strategy of rerouting waste heat from the engine to the adsorbent when the tank nears discharge, driving off the residual methane, thereby increasing the deliverable capacity. The heat-rerouting deliverable capacity given a heating temperature of T_f is then:

$$\sigma(P_H, T_0) - \sigma(P_L, T_f), \quad (\text{S4})$$



(a)

Figure S7. Methane adsorption isotherms calculated for a sample structure with simulations (points) against the extrapolations from the model in eqn S1 that was fit to the 298 K isotherm (solid lines) for varying temperatures.

where the loading $\sigma(P, T)$ is given by the model in eqn S1 and the scalings in eqn S3 are taken into account for the second term. We took into account the temperature-dependence of the fugacity through the Peng-Robinson equation of state.

Fig. S10 shows the heat-rerouting deliverable capacity distributions broken down into material classes for $T_f = 400$ K in comparison to the isothermal deliverable capacity considered by ARPA-E. Also shown is the extreme limit of exploiting the temperature-dependence of the isotherms: at best, this heat-rerouting strategy will drive off all residual methane gas at the discharge, and the heat-rerouting deliverable capacity becomes the loading at P_H as $T_f \rightarrow \infty$. In none of these scenarios do we reach the ARPA-E target.

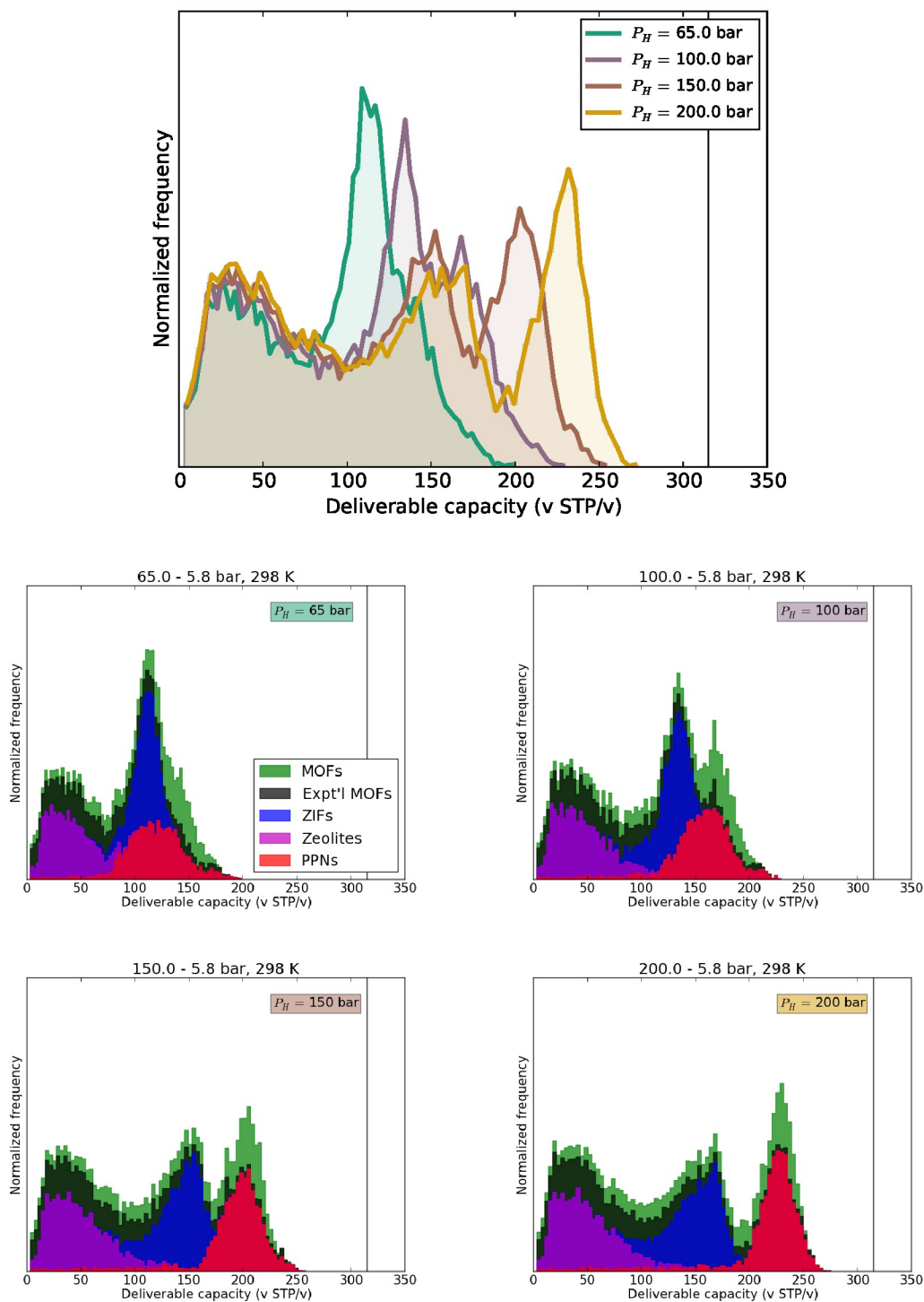


Figure S8. Changing the storage pressure: deliverable capacity of methane for materials operating between pressure P_H and 5.8 bar. [Top] Deliverable capacity distributions under differing P_H . [Bottom] For each scenario, the distribution is partitioned into material classes. The vertical line is the ARPA-E target.

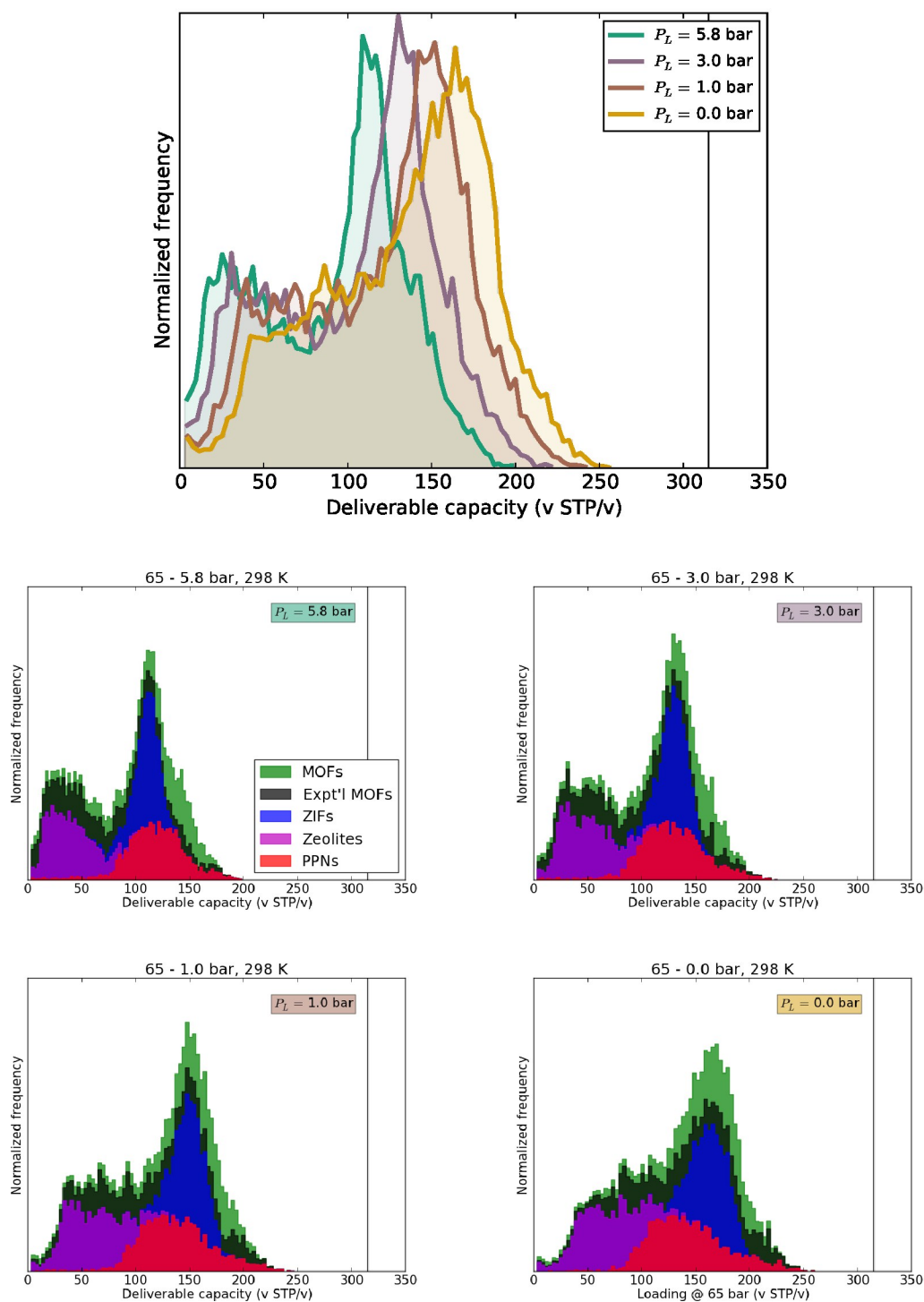


Figure S9. Changing the discharge pressure: deliverable capacity of methane for materials operating between pressure 65 and P_L bar. [Top] Deliverable capacity distributions under differing P_L . [Bottom] For each scenario, the distribution is partitioned into material classes. The vertical line is the ARPA-E target.

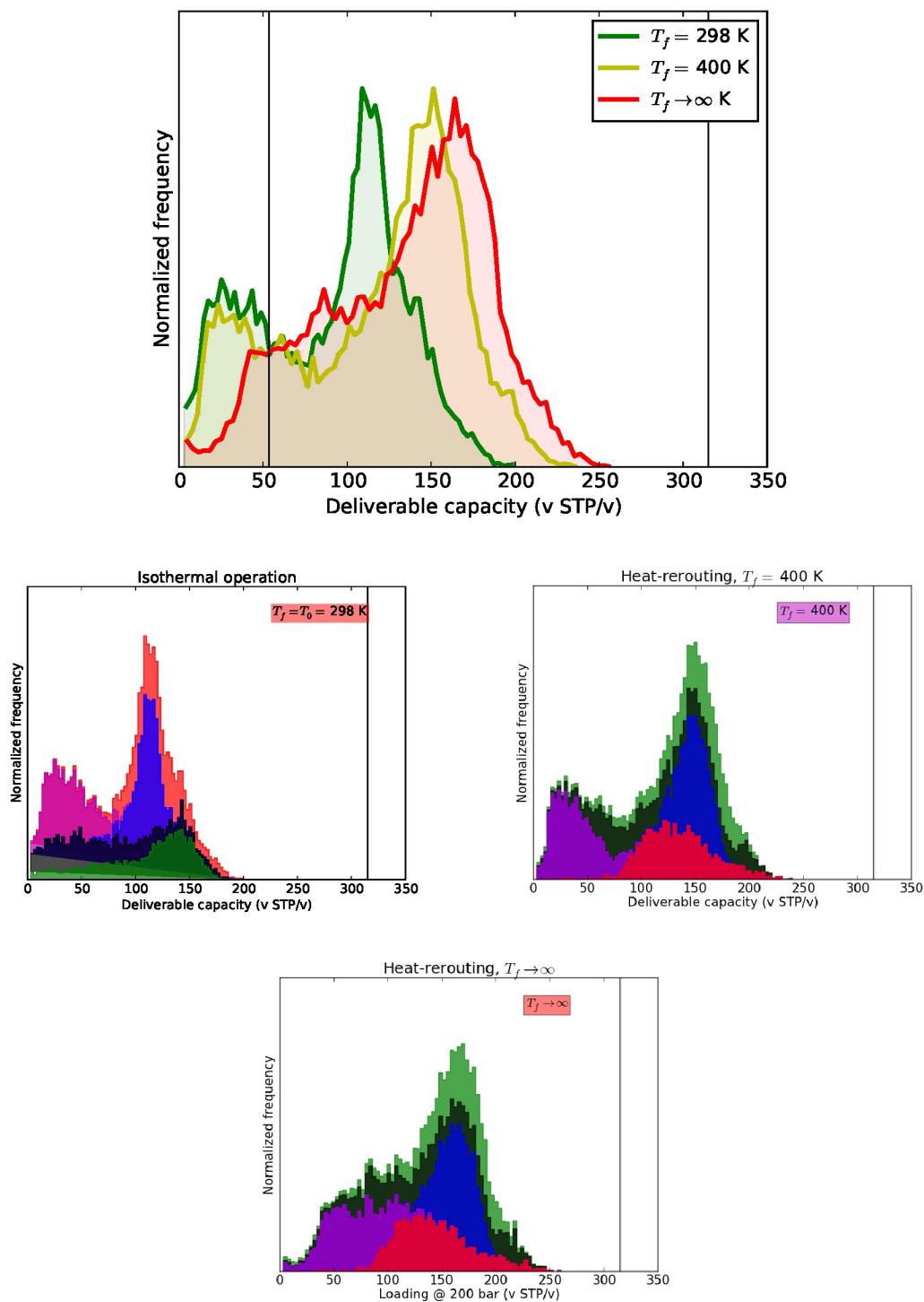


Figure S10. Heat-rerouting deliverable capacity. [Top] Heat-rerouting deliverable capacity where the adsorbent is heated to a temperature T_f when the tank nears discharge. [Bottom] For each scenario, the distribution is partitioned into material classes. The vertical line is the ARPA-E target.

S7 Additional data

In the main text, Fig. 4 shows the relationship between the deliverable capacity and the crystal density. In Fig. S11 we reproduce the same figure but now color-coded by the fractional deliverable capacity. This figure illustrates that (i) the materials with the highest deliverable capacities also have the highest fractional deliverable capacities, and (ii) a high fractional deliverable capacity does not necessarily translate to a high deliverable capacity.

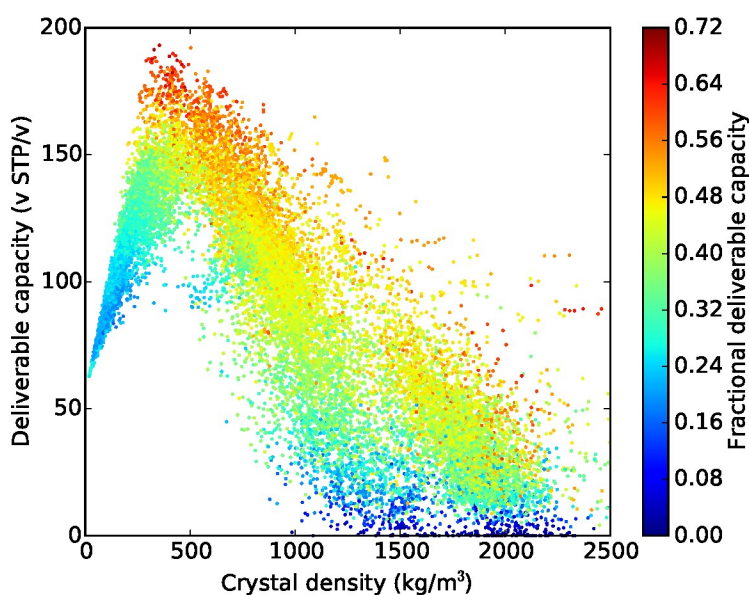
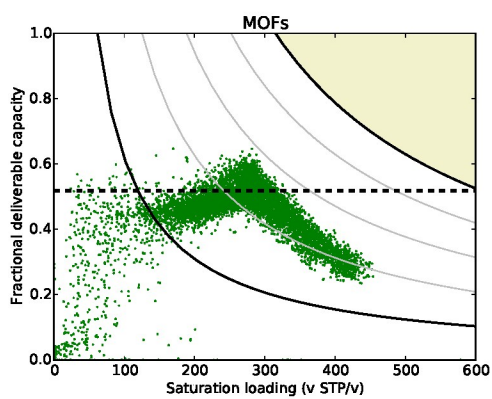


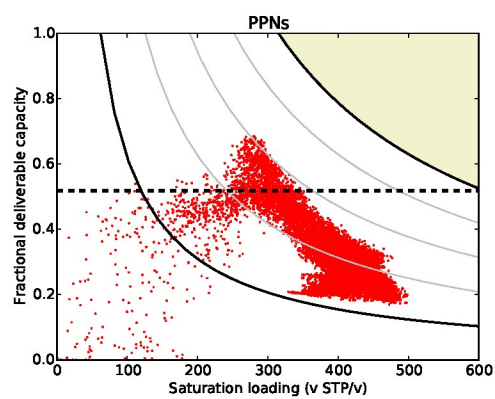
Figure S11. Materials with the highest deliverable capacities indeed have the highest fractional deliverable capacities. Deliverable capacity plotted against the crystal density. Points are color-coded according to fractional deliverable capacity.

In Fig. 5 of the main text, we plotted the fractional deliverable capacity against the saturation loading of all materials in one figure. In Fig. S12, we present this plot separately for each class of material. In addition, the dashed horizontal line marks the theoretical upper bound if a material would be described with a Langmuir isotherm [5]. Above this theoretical upper bound, we find materials that cannot be described with a Langmuir isotherm due to, for example, methane-methane interactions.

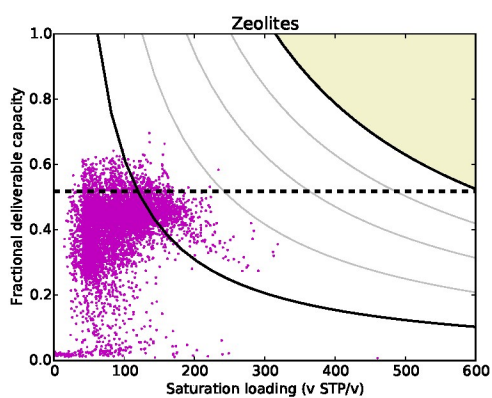
Fig. S13 gives the diameter of the largest included sphere as a function of the crystal density.



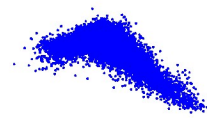
(a)



(b)



(c)



(d)

